

Identification and adaptive control of a high-contrast focal plane wavefront correction system

He Sun^{a,*}, N.Jeremy Kasdin^a, Robert Vanderbei^{a,b}

^aDepartment of Mechanical and Aerospace Engineering, Princeton University, NJ, the United States.

^bDepartment of Operation Research and Financial Engineering, Princeton University, NJ, the United States.

Abstract. All coronagraphic instruments for exoplanet high-contrast imaging need wavefront correction systems to reject optical aberrations and create sufficiently dark holes. Since the most efficient wavefront correction algorithms (controllers and estimators) are usually model-based, the modeling accuracy of the system influences the ultimate wavefront correction performance. Currently, wavefront correction systems are typically approximated as linear systems using Fourier optics. However, the Fourier optics model is usually biased due to inaccuracies in the layout measurements, the imperfect diagnoses of inherent optical aberrations, and a lack of knowledge of the deformable mirrors (actuator gains and influence functions). Moreover, the telescope optical system varies over time because of instrument instabilities and environmental influence. In this paper, we present an expectation-maximization (E-M) approach for identifying and real-time adapting the linear telescope model from data. By iterating between the E-step, a Kalman filter and a Rauch smoother, and the M-step, analytical or gradient based optimization, the algorithm is able to recover the system even if the model depends on the electric fields, which are unmeasurable hidden variables. Simulations and experiments in Princeton’s High Contrast Imaging Lab demonstrate that this algorithm improves the model accuracy and increases the efficiency and speed of the wavefront correction.

Keywords: Exoplanet direct imaging, coronagraph, wavefront correction, E-M algorithm, system identification, adaptive control, reinforcement learning.

*He Sun, hesun@princeton.edu

1 Introduction

In the upcoming era of 30-meter ground-based telescopes and new advanced space telescopes, direct imaging is believed to be the next frontier in exoplanet detection and characterization. Unlike indirect detection methods, such as radial velocity and transit, direct imaging collects light from the planet itself rather than its host star, thus enabling the spectral characterization of the planet’s atmosphere and the full determination of its orbital parameters. But exoplanets are much fainter than their parent stars, requiring the stellar halo to be managed to make high contrast imaging of the exoplanet possible.

A leading technology for achieving the high-contrast needed for exoplanet imaging is the coronagraph.¹⁻⁴ Consisting of a series of optimally designed masks and stops, the coronagraph is able to suppress the spread of starlight, and thus create high-contrast detection regions, so-called dark holes, in the image plane. However, since the coronagraphs are designed assuming perfect optics, they are fundamentally sensitive to any wavefront perturbations. To maintain a high contrast for exoplanet observations, wavefront correction is required for all coronagraph instruments. In a ground-based telescope, the wavefront correction system typically places a wavefront sensor, such as a spatially filtered Shack-Hartmann sensor or a pyramid sensor,^{5,6} in the pupil plane to measure the wavefront aberrations and then directly compensates for them using deformable mirrors (DMs). Such a system is able to cancel pupil phase aberrations due to atmospheric turbulence and achieve contrasts of 10^{-5} to 10^{-6} on current telescopes, allowing for the imaging of young, hot gas giant planets.⁷ Directly imaging dimmer planets, down to Earth size, at higher contrast requires

a space telescope (reaching contrasts below 10^{-8} before post-processing).^{8,9} For these coronagraphs, the pupil plane approach with a separate wavefront sensor is not capable of reaching the highest contrast values because of non-common-path errors. Instead, the focal-plane electric field is estimated using only camera images and then control signals for the DMs are computed based on this estimated field. This estimation and control problem is commonly referred to as focal-plane wavefront correction (FPWC). Effective FPWC algorithms require efficient estimation algorithms and accurate models of the optical system, particularly of the influence of DM voltage commands on the focal-plane electric field.

In all current FPWC systems, the optical models needed for control have been derived by applying Fourier optics to the optical layout. However, inaccuracies in measurements of the optical system, imperfect knowledge of the systematic optical aberrations, and poor or biased models of the DM influence, result in significant bias errors using only the Fourier optics approach. This has a detrimental effect on the wavefront correction speed and the final achievable contrast. This suggests that applying system identification techniques to the FPWC problem could improve the accuracy of the model and thus the overall performance of the system. Classical system identification approaches include phase retrieval^{10,11} and laser interferometric DM surface characterization.¹² In this paper, we propose a new data-driven framework using the expectation-maximization (E-M) algorithm to accurately identify and adaptively control the FPWC system. In contrast to classical approaches, our method does not require a change to the optical system design, tracks real-time systematic changes, and speeds up convergence of the controller.

In the following sections, we first provide a brief overview of the focal plane wavefront correction system, including mathematical modeling and past works on wavefront estimation, control, and system identification. In addition, we also propose a new formalism to formulate the problem as a stochastic optimization problem. Then we review the E-M algorithm and derive the E-M equations of the FPWC system. We finally report the simulation and experimental results on the FPWC system identification and adaptive control in the Princeton High Contrast Imaging Lab (HCIL) to demonstrate the method's ability.

2 Overview of high-contrast focal plane wavefront correction

2.1 Mathematical modeling

The FPWC system in a coronagraph is typically formulated as a state-space model for the convenience of control applications. In this state-space formula, the control inputs, observations and state variables are respectively the DM voltage commands, camera images, and the focal plane electric fields. We begin this section by deriving this underlying state-space model.

The block diagram in Fig. 1 shows the architecture of the telescope optics and the control loop. We define \tilde{E}_0 as the complex incident electric field before the DMs and $\Delta\phi_m$ as the phase change introduced by the DMs at correction iteration m , where (x, y) are the coordinates in the DM plane. The coronagraph operator $\mathcal{C}\{\cdot\}$ represents the propagation from the DM to the focal plane camera. After k correction iterations, the focal plane electric field is given by,

$$E_k = \mathcal{C}\{\tilde{E}_0 e^{i \sum_{m=1}^k \Delta\phi_m}\}. \quad (1)$$

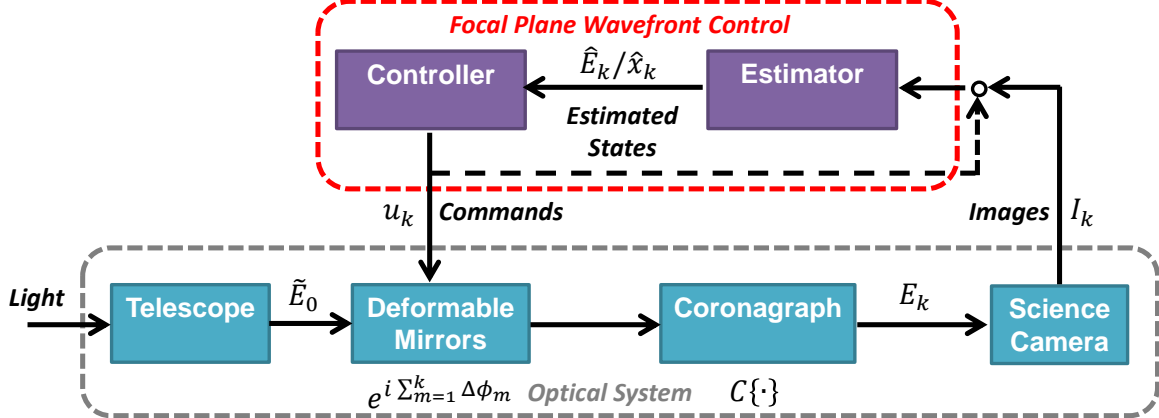


Fig 1 Telescope optical system architecture and focal plane wavefront control loop. System variables are also marked on the diagram, where \tilde{E}_0 is the incident pupil plane electric field, $\Delta\phi_m$ is the DM surface phase change at a single step, $\mathcal{C}\{\cdot\}$ represents the light propagation through coronagraph, E_k is the focal plane electric field, I_k represents the camera images, u_k represents the DM commands, and \hat{E}_k/\hat{x}_k are the estimated complex/real-valued states of electric field.

Since the change in phase due to the DM is assumed small at each step of the controller, the focal plane electric field in Eq. 1 can be expanded in a Taylor series about $\Delta\phi_m$ to yield

$$\begin{aligned} E_k &\approx \mathcal{C}\{\tilde{E}_0\} + \sum_{m=1}^k \mathcal{C}\{\tilde{E}_0 i \Delta\phi_m\} \\ &= E_{k-1} + \mathcal{C}\{\tilde{E}_0 i \Delta\phi_k\}. \end{aligned} \quad (2)$$

where we used the fact that the coronagraph is a linear operator in the applied electric field (as it is composed of Fresnel propagations, Fourier transforms, and coronagraph mask multiplications).

The DM phase change, $\Delta\phi_k$, at each step is approximated by summing weighted influence functions produced by each actuator on the DM. That is, given an influence function, $f_q(x, y)$, which represents the q -th actuator's response to a unit voltage input, the DM induced phase change across the pupil from voltage commands, $u_{k,q}$, is approximated by the linear superposition

$$\Delta\phi_k \approx \sum_{q=1}^{N_{act}} u_{k,q} f_q, \quad (3)$$

where N_{act} is the number of DM actuators.

Substituting Eq. 3 into Eq. 2 results in a linear relationship between the focal plane electric field and the DM voltage commands,

$$E_k = E_{k-1} + \sum_{q=1}^{N_{act}} u_{k,q} \mathcal{C}\{\tilde{E}_0 i f_q\}. \quad (4)$$

By discretizing and vectorizing the 2-D electric fields, Eq. 4 can be put in the common matrix

form of the state transition model,

$$E_k = E_{k-1} + F(\tilde{E}_0, f_{1:N_{act}})u_k, \quad (5)$$

where $E_k, E_{k-1} \in \mathbb{C}^{N_{pix} \times 1}$ are the complex state vectors, $u_k \in \mathbb{R}^{N_{act} \times 1}$ is the DM control input vector, $F \in \mathbb{C}^{N_{pix} \times N_{act}}$ is the system Jacobian matrix, and N_{pix} is the number of camera pixels in the dark holes. The corresponding intensity on the science camera is,

$$I_k = E_k^* \circ E_k, \quad (6)$$

where \circ represents the element-wise multiplication and \star denotes complex conjugation. Eq. 5 and Eq. 6 are, respectively, the state transition and observation equation of the state-space model.

Since the measurement Eq. 6 is the sum of the squares of the real and imaginary components, it is impossible to extract the full complex electric field from a single measurement. Instead, the current approach is to apply n ($n \geq 2$) positive and negative “probe” commands to the DM, denoted by $u_k^p = [u_k^{p,1}, \dots, u_k^{p,n}]$, which result in the set of $2n$ intensity measurements,

$$\begin{aligned} I_k^{m+} &= (E_k + Fu_k^{p,m})^* \circ (E_k + Fu_k^{p,m}), \quad \forall m = 1, \dots, n \\ I_k^{m-} &= (E_k - Fu_k^{p,m})^* \circ (E_k - Fu_k^{p,m}), \quad \forall m = 1, \dots, n. \end{aligned} \quad (7)$$

These are then subtracted to form an overdetermined set of n linear measurements of the electric field,

$$\begin{bmatrix} \Delta I_k^1 \\ \vdots \\ \Delta I_k^n \end{bmatrix} = \begin{bmatrix} I_k^{1+} - I_k^{1-} \\ \vdots \\ I_k^{n+} - I_k^{n-} \end{bmatrix} = \Re \left\{ \begin{bmatrix} 4(Fu_k^{p,1})^* \circ E_k \\ \vdots \\ 4(Fu_k^{p,n})^* \circ E_k \end{bmatrix} \right\} = \Re \left\{ \begin{bmatrix} 4\text{diag}\{(Fu_k^{p,1})^*\} \\ \vdots \\ 4\text{diag}\{(Fu_k^{p,n})^*\} \end{bmatrix} E_k \right\}, \quad (8)$$

where $\text{diag}\{\cdot\}$ represents the diagonal matrix constructed from a vector. Equations 5 and 8 make up the linear state-space model of the FPWC system.

The element-wise product structure in Eq. 8 decouples the linear state transition equations in each pixel, so the electric field of a single pixel can be estimated based only on its own intensity measurements. For mathematical convenience, we can further split the real and imaginary part of the electric field and derive real-valued state-space equations,

$$\begin{aligned} x_{k,j} &= x_{k-1,j} + G_j u_k, \\ z_{k,j} &= H_{k,j} x_{k,j}, \end{aligned} \quad (9)$$

where $j \in \{1, \dots, N_{pix}\}$ is the index of camera pixels, and

$$x_{k,j} = \begin{bmatrix} \Re\{E_{k,j}\} \\ \Im\{E_{k,j}\} \end{bmatrix}, G_j = \begin{bmatrix} \Re\{F_{j,1:N_{act}}\} \\ \Im\{F_{j,1:N_{act}}\} \end{bmatrix}, z_{k,j} = \begin{bmatrix} \Delta I_{k,j}^1 \\ \vdots \\ \Delta I_{k,j}^n \end{bmatrix}, H_{k,j} = 4(G_j u_k^p)^T. \quad (10)$$

The elements of the state vectors and matrices are now real numbers, which is more convenient for developing estimators and system identification algorithms.

2.2 Focal plane wavefront estimation and control

With the state-space model developed in Sec. 2.1, we now introduce the wavefront estimation and control algorithms. The baseline wavefront estimation approach used in most implementations to date is the least-square, batch process estimator (BPE),^{13,14} which can be derived as follows. We begin with the linear observation model in Eq. 9 but with an additive noise term, $n_{k,j}$, to represent camera measurement noise and observation matrix errors (originally from Jacobian matrix errors),

$$z_{k,j} = H_{k,j}x_{k,j} + n_{k,j}, \quad (11)$$

where $n_{k,j} \sim \mathcal{N}(0, R_{k,j})$ is the added measurement noise assumed to follow a Gaussian distribution. We can then perform a least-square regression to estimate the expectation, $\hat{x}_{k,j}$, and the covariance matrix, $P_{k,j}$, of the state vector at each time step, k ,

$$\begin{aligned} \hat{x}_{k,j} &= (H_{k,j}^T H_{k,j})^{-1} H_{k,j}^T z_{k,j}, \\ P_{k,j} &= (H_{k,j}^T H_{k,j})^{-1} H_{k,j}^T R_{k,j} H_{k,j} (H_{k,j}^T H_{k,j})^{-1}. \end{aligned} \quad (12)$$

Repeating this regression procedure for all pixels provides an estimate of the entire electric field in the focal plane. While this algorithm is easy to implement, the estimation accuracy, indicated by the estimation covariance, is fully determined by the measurement noises. When the signal-noise-ratio (SNR) is low (which happens as the dark hole improves), this batch process estimator cannot provide accurate enough estimates to be used for control.

A better solution is to incorporate prior knowledge from the model and previous measurements using a Kalman filter.¹⁵ This formulation allows us to introduce a process noise term to the state-space equations to represent Jacobian matrix bias errors in instabilities in the system,

$$x_{k,j} = x_{k-1,j} + G_j u_k + w_{k,j}, \quad (13)$$

where $w_{k,j} \sim \mathcal{N}(0, Q_{k,j})$ is the additive Gaussian process noise. At control iteration k , the state transition model provides a prediction of the current state, since we have $\hat{x}_{k-1,j}$ and $P_{k-1,j}$ from the previous estimation. With this prior knowledge, we can derive the log-likelihood function of the current state and the observations,

$$\begin{aligned} \log p(z_{k,j}, x_{k,j}) &= -\frac{1}{2}(x_{k,j} - \hat{x}_{k,j|k-1})^T P_{k,j|k-1}^{-1} (x_{k,j} - \hat{x}_{k,j|k-1}) \\ &\quad - \frac{1}{2}(z_{k,j} - H_{k,j}x_{k,j})^T R_{k,j}^{-1} (z_{k,j} - H_{k,j}x_{k,j}), \end{aligned} \quad (14)$$

where

$$\begin{aligned} \hat{x}_{k,j|k-1} &= \hat{x}_{k-1,j} + G_j u_k, \\ P_{k,j|k-1} &= H_{k,j} P_{k,j} H_{k,j}^T + R_{k,j} \end{aligned} \quad (15)$$

are respectively the a-priori state and covariance estimates and $p(z, x)$ is the joint probability density function for z and x . The Kalman filter maximizes this log-likelihood function, so it optimally combines the information from the model and the observations and thus reduces the estimation covariance.

Recently, Riggs et al.¹⁶ introduced an incoherent light term into the nonlinear observation

model, Eq. 6,

$$I_k = E_k^* \circ E_k + I_{inco,k}. \quad (16)$$

They then employed an extended Kalman filter (EKF) to simultaneously estimate both the coherent electric field and incoherent intensity (which contains the planet). This method removes the requirement for pair-wise probing and makes simultaneous wavefront correction and planet detection possible. This EKF approach is not used in this paper, however, it will be applied to improve the system identification work described here in a future paper to characterize system nonlinearities.

With the state estimates available, it is now possible to compute the DM voltage commands to manipulate the focal plane electric field. For mathematical simplicity, we construct a real, linear state transition model by combining the state equations for each pixel (Eq. 13) into a single vectorized form,

$$x_k = x_{k-1} + Gu_k + w_k, \quad (17)$$

where

$$x_k = \begin{bmatrix} x_{k,1} \\ \vdots \\ x_{k,N_{pix}} \end{bmatrix}, G = \begin{bmatrix} G_1 \\ \vdots \\ G_{N_{pix}} \end{bmatrix}, w_k = \begin{bmatrix} w_{k,1} \\ \vdots \\ w_{k,N_{pix}} \end{bmatrix}. \quad (18)$$

The controller must drive the state x_k as close to zero as possible to maintain a high contrast in the dark hole. Currently, the two most popular model-based optimal controllers are electric field conjugation (EFC)¹⁷ and stroke minimization (SM).¹⁸

EFC works by minimizing a cost function consisting of the total energy in the dark holes and a Tikhonov regularization, which can be written,

$$\min_{u_k} \quad x_k^T x_k + \alpha_k u_k^T u_k, \quad s.t. \quad x_k = x_{k-1} + Gu_k, \quad (19)$$

where α_k is the Tikhonov regularization parameter.

In contrast, stroke minimization aims to find the smallest DM commands that achieve a target contrast, which can be formulated as the constrained minimization,

$$\min_{u_k} \quad u_k^T u_k, \quad s.t. \quad x_k^T x_k = C_k, \quad x_k = x_{k-1} + Gu_k, \quad (20)$$

where C_k is the target contrast, or total energy, in the dark holes. The equality constraints can be incorporated into the cost function via a Lagrange multiplier, making stroke minimization into a similar formula to EFC,

$$\min_{u_k} \quad u_k^T u_k + \mu_k (x_k^T x_k - C_k), \quad s.t. \quad x_k = x_{k-1} + Gu_k. \quad (21)$$

The optimal solutions of Eq. 20 and Eq. 21 give two corresponding feedback control laws,

$$u_k = -(G^T G + \alpha_k \mathbb{I})^{-1} G^T x_{k-1} \quad \text{and} \quad u_k = -(G^T G + \frac{1}{\mu_k} \mathbb{I})^{-1} G^T x_{k-1}. \quad (22)$$

where $\mathbb{I} \in \mathbb{R}^{N_{act} \times N_{act}}$ is the identity matrix.

It is evident that EFC and stroke minimization, as more rigorously discussed by Groff et al.,¹⁹ in fact define the same control law except for the tuning parameters, α_k , and the Lagrange multiplier, μ_k . The Lagrange multiplier, μ_k , is a function of the target contrast C_k , which is the tuning parameter in stroke minimization. Both α_k and μ_k introduce a damping term, although based on different considerations, in the matrix inversion, which helps avoid an ill-posed matrix inversion problem and, more importantly, reduce the influence of Jacobian matrix biases. Tuning the damping parameter, α_k and μ_k , which turns out to be non-trivial, is the key to properly implementing the controllers.²⁰

2.3 System identification

Because the wavefront estimators and controllers are all model-based, performance can be improved by implementing system identification techniques that improve knowledge of the underlying model. To date, all system identification approaches work to identify the Jacobian matrix in the linear formulation.

As indicated by Eq. 5, the Jacobian matrix is fundamentally a function of the incident electric field, \tilde{E}_0 , and the actuator influence functions, $f_{1:N_{act}}$, so an indirect approach to identifying the model is to characterize \tilde{E}_0 and $f_{1:N_{act}}$ separately and then compute the Jacobian matrix based on the coronagraphic propagation equations. The influence functions are usually characterized using laser interferometry.¹² Since it is too time consuming to measure the surface responses of all the actuators (several thousands on each DM), typically only a few representative actuators are characterized with the assumption that all actuators have similar responses. The incident electric field, though, cannot be directly measured. It is typically reconstructed from multiple focused and defocused images using phase retrieval algorithms.²¹ However, all the phase retrieval algorithms assume a certain light propagation model, so they do not have the ability to diagnose any errors from an incorrect optical layout prescription. In addition, since the coronagraph typically blocks most of the light from the entrance pupil, there are very few photons to provide the needed information. To fix this, current system identification approaches remove the coronagraph for the identification step; this makes the identification time consuming and prone to non-common path error.

Recent work by Zhou et al. abandoned a physics-based approach for determining the Jacobian matrix in favor of directly identifying the Jacobian matrix by perturbing the DM shapes and observing the resulting camera images.²² The physical interpretation of a Jacobian matrix column is the influence of a DM actuator with unit voltage command on the focal plane electric field. Therefore, by definition, the Jacobian matrix can be derived by commanding each actuator and estimating the focal plane electric field changes. The least-squared, batch process estimator (BPE) was employed in that work for the electric field estimation. However, since BPE requires a large amount of data and is relatively noisy, the identification procedure was time consuming and the resulting identified model was too noisy to be used in the wavefront correction. In addition, the identified model using BPE was also limited by the initial knowledge of the Jacobian matrix. Therefore, up to now, this work has only been used for qualitatively understanding the sources of the model errors, instead of quantitatively correcting the Jacobian matrix errors. In the remainder of this paper we present an alternative approach to modeling the system and implementing a quantitatively useful system identification.

3 FPWC as a stochastic optimization problem

As can be seen from Sec. 2, the typical approach to focal-plane wavefront control is to examine the wavefront estimation, wavefront control, and system identification as separate problems. In this section, we introduce a new way to formulate the FPWC problem as a single stochastic optimization problem. As first shown by Sun et al.,²³ this approach provides better physical insights into the tuning parameters in the algorithms and also explains how the wavefront control, estimation, and system identification influence the final contrast in the dark hole.

The ultimate goal of the FPWC is to minimize the total intensity, $x_k^T x_k$, in the dark holes. Since the state, x_k , is a random variable, we can formulate FPWC as a stochastic optimization/control problem that minimizes the expectation of the dark hole intensity, $\langle x_k^T x_k \rangle$. The state variable follows the stochastic process in Eq. 17. With the assumption that the process noise, w_k , has a zero mean, the expectation at step k can be distributed as

$$\begin{aligned} \langle x_k^T x_k \rangle &= \langle x_{k-1}^T x_{k-1} \rangle + 2 \langle x_{k-1} \rangle^T G u_k + u_k G^T G u_k + \langle w_k^T w_k \rangle \\ &= \langle x_{k-1}^T \rangle \langle x_{k-1} \rangle + 2 \langle x_{k-1} \rangle^T G u_k + u_k G^T G u_k + \langle w_k^T w_k \rangle + \sum_{j=1}^{N_{pix}} \text{Tr}(\text{var}(x_{k-1,j})) \end{aligned} \quad (23)$$

The statistics of the previous state are provided by the wavefront estimation, $\langle x_{k-1} \rangle = \hat{x}_{k-1}$ and $\text{var}(x_{k-1,j}) = P_{k-1,j}$. The process noise term is determined empirically and models the Jacobian matrix errors ΔG , i.e., $w_k \cong \Delta G u_k$.¹ The process noise term in Eq. 23 thus becomes $\langle w_k^T w_k \rangle = u_k^T \langle \Delta G^T \Delta G \rangle u_k$, where $\langle \Delta G^T \Delta G \rangle \triangleq W$ models Jacobian uncertainties. The stochastic optimization problem can now be written

$$\min \quad \hat{x}_{k-1}^T \hat{x}_{k-1} + 2 \hat{x}_{k-1}^T G u_k + u_k G^T G u_k + u_k^T W u_k + \sum_{j=1}^{N_{pix}} \text{Tr}(P_{k-1,j}). \quad (24)$$

As this cost function indicates, the final contrast depends on not only the DM commands, u_k , but also the estimation accuracy, $\text{Tr}(P_{k-1,j})$, and the model uncertainties, W . Minimizing the first four terms of the cost function over u_k defines the wavefront controller, while minimizing the trace of the estimation covariance matrix over \hat{x}_{k-1} defines the wavefront estimator. In addition, system identification or adaptive control can be used to reduce the model uncertainties, $\text{Tr}(W) = \|\Delta G\|_F^2$, which also improves the final achievable contrast from the wavefront correction.

By definition, the entries of the regularization matrix are

$$W_{m,l} = \sum_{j=1}^{N_{pix}} \langle \Delta G_{j,m}^T \Delta G_{j,l} \rangle, \quad \Delta G_j \in \mathbb{R}^{2 \times N_{act}}, \forall j = 1, \dots, N_{pix}, \quad (25)$$

where the subscripts, m and l , represent the column indices of the matrices. Each column of ΔG gives the modeling errors of an actuator's influence, so $W_{m,l}$ indicates the covariance of Jacobian

¹In fact, the process noise, $w_k \cong \Delta G u_k + r_k$, which should also include another random noise term, r_k , not related to the Jacobian, from errors such as the DM drift. However, when the Jacobian errors are larger than other influences, the random noise term is neglectable. We will discuss the influence of the DM drift errors in our future papers.

errors from the m -th and l -th actuators. In general, W is a symmetric positive definite matrix with nearly all the entries non-zeros.

The off-diagonal entries in W disappear if different actuators are assumed to be uncoupled from each other. EFC or SM with scalar regularization further assume that the covariance of errors from different actuators are identical. Thus, given that

$$\begin{aligned}\langle \Delta G_{j,m}^T \Delta G_{j,m} \rangle &= \text{Tr}(\text{var}(\Delta G_{j,m})) = 2\sigma^2, \forall j, m, \\ \langle \Delta G_{j,m}^T \Delta G_{j,l} \rangle &= \text{Tr}(\text{cov}(\Delta G_{j,m}, \Delta G_{j,l})) = 0, \forall j, m \neq l,\end{aligned}\quad (26)$$

W degrades to a scaled identity matrix,

$$W = 2N_{pix}\sigma^2\mathbb{I}. \quad (27)$$

This shows that tuning the Tikhonov regularization parameter or Lagrange multiplier is equivalent to finding the magnitude of Jacobian uncertainties in our model. A smaller regularization parameter indicates smaller Jacobian errors, which finally leads to higher contrast according to Eq. 24. In the following sections, we will explore the system identification and the adaptive control using only a scalar regularization assumption. Characterizing the filled regularization matrix turns out to be very hard, because the high-dimensional system it suggests is usually underdetermined and requires tremendous amount of data for identification. To proceed with this idea, we have to assume some known structure of the regularization matrix to reduce the number of adaptable parameters.²

4 Expectation-Maximization (E-M) algorithm

The new stochastic optimization formulation in Sec. 3 indicates the potential from model identification for improving the wavefront corrections. Moreover, it indicates not only that identifying the Jacobian matrix is necessary, but also that characterizing the process and observation noises are important for tuning the optimal estimators and controllers. In this section, we develop a new E-M algorithm based system identification approach²⁴ to accomplish all of these goals.

4.1 Review of the E-M algorithm

The E-M algorithm is an iterative procedure to find the maximum a posteriori (MAP) estimates of the model parameters in the presence of hidden variables.²⁵ For example, in focal plane wavefront correction, the state-space model includes the DM control and probing commands, the camera images, and the focal plane electric fields, which are respectively the model inputs, the model outputs, and the unobservable hidden variables of the system. Since the true values of the hidden variables are absent, we cannot explicitly derive the log-likelihood function and apply the maximum likelihood estimation (MLE) to identify the model parameters. Instead, we maximize a lower bound of the log-likelihood of only the model inputs and outputs. In general, with the hidden variables, the model inputs and outputs (usually referred to as the training data), and the model parameters, denoted as X , Y and θ respectively, the log-likelihood can be written as an integral of the marginal probability over the hidden variables,

$$\mathcal{L}\{\theta\} = \log p(Y|\theta) = \log \int p(X, Y|\theta) dX. \quad (28)$$

²For example, we can assume only neighboring actuators are coupled, which makes the matrix very sparse.

Assuming an arbitrary probability distribution of the hidden variables $\mathcal{Q}(X)$, a lower bound on the log-likelihood, $\mathcal{F}(\mathcal{Q}, \theta)$, can be bounded using Jensen's inequality,

$$\mathcal{L}\{\theta\} = \log p(Y|\theta) = \log \int p(X, Y|\theta) dX \quad (29a)$$

$$= \log \int \mathcal{Q}(X) \frac{p(X, Y|\theta)}{\mathcal{Q}(X)} dX \quad (29b)$$

$$\geq \int \mathcal{Q}(X) \log \frac{p(X, Y|\theta)}{\mathcal{Q}(X)} dX \quad (29c)$$

$$= \int \mathcal{Q}(X) \log p(X, Y|\theta) dX - \int \mathcal{Q}(X) \log \mathcal{Q}(X) dX \quad (29d)$$

$$= \mathcal{F}(\mathcal{Q}, \theta). \quad (29e)$$

The E-M algorithm alternates between maximizing this lower bound with respect to the hidden variable distribution, $\mathcal{Q}(X)$, and the model parameters, θ . Computing the distribution $\mathcal{Q}(X)$ while fixing θ is called the expectation-step (E-step), and computing the model parameters θ while fixing $\mathcal{Q}(X)$ is called the maximization-step (M-step). Theoretically, the model parameter estimation always converges to a local minimum after enough iterations of the E-step and the M-step.

4.2 Derivation of the E-M equations for FPWC system

The dynamics of different pixels are decoupled in the FPWC system under the linear approximation (Eq. 2), so we identify their state-space equations separately in the E-M algorithm. Moreover, this strategy avoids the inversion and multiplication of large matrices, which reduces the computational expense of the algorithm. Here we copy the state transition equation and the pair-wise probing equation defined by Eq. 11 and Eq. 13,

$$\begin{aligned} x_{k,j} &= x_{k-1,j} + G_j u_k + w_{k,j}, \quad w_{k,j} \sim N(0, Q_{k,j}), \\ z_{k,j} &= H_{k,j} x_{k,j} + n_{k,j}, \quad H_{k,j} = 4u_k^{pT} G_j^T, \quad n_{k,j} \sim N(0, R_{k,j}). \end{aligned} \quad (30)$$

where $k \in \{1, \dots, N_d\}$ is the index of the control iterations, $j \in \{1, \dots, N_{pix}\}$ is the index of camera pixels, and N_d is the total number of the control iterations.

Eq. 30 is a typical input-output hidden Markov process. As mentioned before, the hidden variables are the state of the electric fields at all control steps in pixel j , $X_j = \{x_{0:N_{d,j}}\}$. The training data are the DM control commands, the pair-wise probing commands, and the camera difference images, $Y_j = \{u_{1:N_d}, u_{1:N_d}^p, z_{1:N_{d,j}}\}$. The model parameters include not only the Jacobian matrix, G_j , but also the process noise covariance and the observation noise covariance, $Q_{k,j}$ and $R_{k,j}$. Based on the assumption we made for the process noise in Sec. 3, i.e. $w_{k,j} \cong \Delta G_j u_k \in \mathbb{R}^{2 \times 2}$ and the Jacobian errors from different actuators are independent, the process noise covariance matrix is proportional to the DM strokes,

$$Q_{k,j} = u_k^T u_k Q_j = u_k^T u_k \sigma^2 \mathbb{I}_{2 \times 2}, \quad (31)$$

Without changing exposure time, the observation noise covariance matrix is a constant scalar ma-

trix over iterations,

$$R_{k,j} = R_j = \nu^2 \mathbb{I}_{n \times n}, \quad (32)$$

where ν is the standard deviation of the observation noise and n is the number of pairs of probes. As a result, the model parameters are $\theta_j = \{G_j, Q_j, R_j\}$, where Q_j and R_j are scalar matrices.

The E-M equations for X_j , Y_j , and θ_j can be derived following the approach of Ghahramani et al.²⁶ For notational simplicity, we will omit the subscript j in the following derivations and discussions, understanding that the E-step and the M-step are repeated N_{pix} times.

4.2.1 The E-Step

The E-step is maximized when the inequality in Eq. 29(c) becomes an equality, i.e. $\mathcal{L}\{\theta\} = \mathcal{F}(Q, \theta)$. According to Jensen's inequality, the equality holds in Eq. 29(c) if and only if $p(X, Y|\theta)/Q(X)$ is constant for any possible X . The joint probability $p(X, Y|\theta)$ can be rewritten as a conditional probability using Bayes' rule,

$$p(X, Y|\theta) = p(X|Y, \theta)p(Y|\theta). \quad (33)$$

Since $p(Y|\theta)$ does not depend on X , the E-step is maximized when $Q(X) = p(X|Y, \theta)$. This conditional probability can be derived from a combined approach using a Kalman filter and Rauch smoothing. In what follows, we introduce notations $\hat{x}_{k_1|k_2}$ and $P_{k_1|k_2}$, which represent the estimate and covariance of the state variables at control iteration k_1 given observations up to and including at control iteration k_2 .

The Kalman filter first forward propagates the states and estimates the hidden states based only on the data up to the current step. The Kalman filter optimization problem is defined in Sec. 2.2. The solution to the optimization problem gives five Kalman filter equations,

$$\hat{x}_{k|k-1} = \hat{x}_{k-1|k-1} + Gu_k, \quad (34a)$$

$$P_{k|k-1} = P_{k-1|k-1} + Q_k, \quad (34b)$$

$$K_k = P_{k|k-1} H_k^T (H_k P_{k|k-1} H_k^T + R_k)^{-1}, \quad (34c)$$

$$\hat{x}_{k|k} = \hat{x}_{k|k-1} + K_k (z_k - H_k \hat{x}_{k|k-1}), \quad (34d)$$

$$P_{k|k} = (\mathbb{I} - K_k H_k) P_{k|k-1}^{-1}, \quad (34e)$$

where $\hat{x}_{k|k-1}$ and $P_{k|k-1}$ are the a priori knowledge of the states and covariance matrix from observations up to control iteration $k-1$, and $\hat{x}_{k|k}$ and $P_{k|k}$ are the a posteriori estimates updated by the observations at step k .

Rauch smoothing then propagates the states backwards from the last step to the starting step and further updates the estimates based on all the training data. Mathematically, Rauch smoothing is a Kalman filter using the next hidden state as the observation. The Rauch smoothing equations are,

$$L_k = P_{k|k} P_{k+1|k}^{-1}, \quad (35a)$$

$$\hat{x}_{k|N_d} = \hat{x}_{k|k} + L_k (\hat{x}_{k+1|N_d} - \hat{x}_{k+1|k}), \quad (35b)$$

$$P_{k|N_d} = P_{k|k} + L_k (P_{k+1|N_d} - P_{k+1|k}) L_k^T, \quad (35c)$$

where $\hat{x}_{k|N_d}$ and $P_{k|N_d}$ are the estimated hidden state's expectation and covariance based on all the N steps of training data, Y . Under the assumption of Gaussian random variables, $\hat{x}_{k|N_d}$ and $P_{k|N_d}$ define the hidden states' probability distribution, $\mathcal{Q}(X) = p(X|Y, \theta)$, which is what is sought in the E-step.

4.2.2 The M-Step

The M-step is maximized when $\int_X \mathcal{Q}(X) \log p(X, Y|\theta) dX = E_X[\log p(X, Y|\theta)]$, the expectation of the log likelihood, is maximized. Based on the Markovian structure of Eq. 30, the log likelihood of the hidden states and the training data is,

$$\begin{aligned} L(G, Q, R) &= \log \prod_{k=1}^{N_d} p(z_k|x_k, H_k, R_k) \prod_{k=1}^{N_d} p(x_k|x_{k-1}, u_k, G, Q_k) \\ &= -\frac{1}{2} \sum_{k=1}^{N_d} (z_k - H_k x_k)^T R_k^{-1} (z_k - H_k x_k) - \frac{1}{2} \sum_{k=1}^{N_d} \log |2\pi R_k| \\ &\quad - \frac{1}{2} \sum_{k=1}^{N_d} (x_k - x_{k-1} - Gu_k)^T Q_k^{-1} (x_k - x_{k-1} - Gu_k) - \frac{1}{2} \sum_{k=1}^{N_d} \log |2\pi Q_k|. \end{aligned} \quad (36)$$

where

$$R_k = R, \quad Q_k = u_k^T u_k Q, \quad H_k = 4(Gu_k^p)^T \quad (37)$$

The expectation of this log-likelihood can be calculated using the state estimates in the E-step. Therefore, we can estimate the model parameters by taking the derivatives of the log-likelihood with respect to each and forcing the resulting expectations to be zero,

$$\frac{\partial \langle L(G, Q, R) \rangle}{\partial G} = 0, \quad \frac{\partial \langle L(G, Q, R) \rangle}{\partial Q} = 0, \quad \frac{\partial \langle L(G, Q, R) \rangle}{\partial R} = 0. \quad (38)$$

This gives the analytical update equations for the model parameters,

$$G = \left\{ \sum_{k=1}^{N_d} \frac{1}{u_k^T u_k} (\hat{x}_{k|N_d} - \hat{x}_{k-1|N_d}) u_k^T + 4Q \sum_{k=1}^{N_d} [\hat{x}_{k|N_d} z_k^T - 4(\hat{x}_{k|N_d} \hat{x}_{k|N_d}^T + P_{k|N_d}) Gu_k^p] R^{-1} u_k^{pT} \right\} \left(\sum_{k=1}^{N_d} \frac{u_k u_k^T}{u_k^T u_k} \right)^{-1}, \quad (39a)$$

$$Q = \frac{1}{N_d} \sum_{k=1}^{N_d} \frac{1}{u_k^T u_k} [(\hat{x}_{k|N_d} - \hat{x}_{k-1|N_d} - Gu_k)(\hat{x}_{k|N_d} - \hat{x}_{k-1|N_d} - Gu_k)^T + P_{k|N_d} + P_{k-1|N_d}], \quad (39b)$$

$$R = \frac{1}{N_d} \sum_{k=1}^{N_d} [(z_k - 4(Gu_k^p)^T \hat{x}_{k|N_d})(z_k - 4(Gu_k^p)^T \hat{x}_{k|N_d})^T + 16(Gu_k^p)^T P_{k|N_d} Gu_k^p]. \quad (39c)$$

Eq. 39 (a) is an implicit equation, so G needs to be found recursively. From our earlier assumption,

tion, Q and R are forced to be scaled identity matrices,

$$Q \leftarrow \frac{Tr(Q)}{2} \mathbb{I}_{2 \times 2}, \quad R \leftarrow \frac{Tr(R)}{2} \mathbb{I}_{2 \times 2}, \quad (40)$$

where we accordingly obtain

$$\sigma^2 = \frac{Tr(Q)}{2}, \quad \nu^2 = \frac{Tr(R)}{2}. \quad (41)$$

The process covariance, σ^2 , can be used in the EFC algorithm for computing the Tikhonov regularization parameter as shown in Eq. 27.

One shortcoming of this analytical solution is the large matrix inversion in Eq. 39(a). To ensure the matrix is invertible, we have to collect several thousand steps of data before making an update, which is unnecessarily time-consuming and also precludes online system adapting. In order to update the model with a smaller amount of data, we can use a stochastic gradient ascent algorithm instead for updating the Jacobian matrix,

$$G \leftarrow G + \eta \frac{\partial \langle L(G, Q, R) \rangle}{\partial G}, \quad (42)$$

where the tuning parameter η defines the learning rate of the algorithm.

These two subsections presented all of the E-M equations for FPWC identification. By repeating the iterative E-M approach on all the pixels we can reconstruct the linear state-space model for the entire system. While that is sufficient, it is helpful to apply a final step, forcing the process and observation noise matrices of all the pixels to be equal to their average. Since all pixels in the dark hole share almost the same noise distributions, neglecting the small difference in photon noises, this step enhances the robustness of the E-M identification.

5 Numerical verification of the E-M system identification

In this section, we numerically investigate the E-M algorithm for FPWC system identification by simulating the Princeton's High Contrast Imaging Lab (HCIL) testbed. Our goal for the system identification is to precisely characterize the Jacobian errors rather than adapting the control system in real time, so we here first generate all the training data and then run the E-M algorithm. The E-M algorithm based adaptive control will be discussed in Sec. 7.

5.1 Data generation with HCIL setup

As shown in Fig. 2, the HCIL testbed is a two-DM FPWC system with shaped pupil (SP) coronagraph. It utilizes a ripple pupil plane mask to suppress the contrast by changing the starlight point spread function (PSF). In addition, a bowtie shaped focal plane mask (FPM) blocks the center part of the PSF to avoid camera saturation, which also defines the dark hole regions for the FPWC. In our numerical study, we simulate the DM commands and resulting camera images under an imperfect lab condition: optical aberrations are added to the shaped pupil plane and two DM planes, and the DM actuators' influence functions are biased by 20% in amplitude. Poisson and Gaussian noises are added to the simulated images, where the noises' standard deviations are chosen based

on measurements in the HCIL. Without loss of generality, we identify the state-space model of the first DM only. The second DM is treated as a fold mirror. Each DM in the HCIL has 952 actuators.

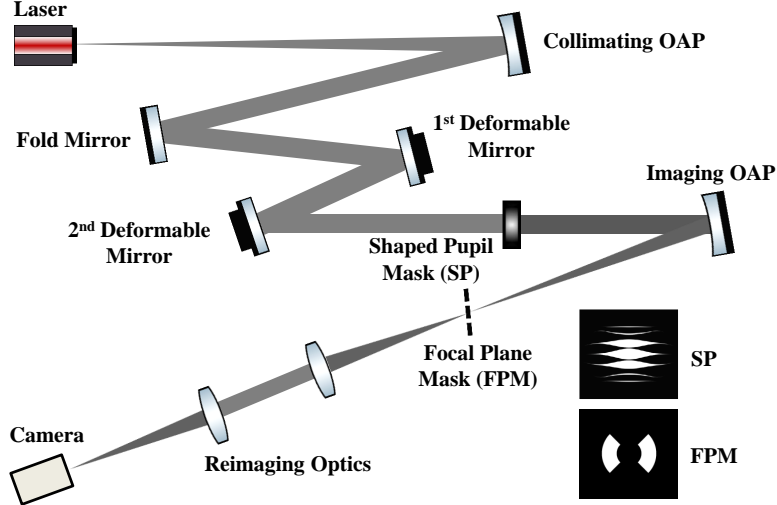


Fig 2 Layout of the HCIL testbed. Rippled shaped pupil and bowtie shaped focal plane mask are applied to suppress the contrast in the focal plane. Two Boston MicroMachines MEMS DMs are installed for focal plane wavefront correction.

To sufficiently explore the controllable space of the DM, we generated the training data by applying random DM commands instead of running wavefront controllers in the system identification approach. In our simulation, in total 4000 random voltage commands (between -0.6 – 0.6 volts) were applied to the DM and the resulting camera images were simulated. A fixed exposure time of 0.1 sec was used for the camera images. For each random DM commands, we collected two pairs of probing images, so we have in total 16000 images (2 images/pair \times 2 pairs/command \times 4000 commands) in our training set. The random commands between -0.6 and 0.6 volts typically result in contrast changes at a level of 1×10^{-6} . In order to make the DM influence significant enough for learning so that the effect is larger than the background speckles, in our simulation, we first ran wavefront control for four steps to reach a contrast of roughly 3×10^{-6} and then applied the random DM commands and generated the images. During the entire control procedure, we used the same probe commands for all 4000 data points. Although identical pair-wise probes are not necessary for the E-M system identification, as will be discussed, it helps us build a metric to evaluate the effectiveness of the identification.

5.2 System identification results

We applied both the analytical method and the stochastic gradient ascent method to the simulated data and investigated the influence the number of data points had on the identification accuracy; the results are described in this section. For the gradient ascent identification, we also examined the effect of using different batch sizes. The batch size is a machine learning term referring to the number of training points utilized in one EM update. Given a batch size, we can divide the training data into many subsets with the same amount of data, and sequentially run the EM algorithm on each subset until all the data is used. Theoretically, small batch sizes enable timely model parameter updates, but sacrifice the accuracy of each update (because the hidden state estimation

in the E-Step is not accurate with a small amount of data). Large batch sizes are more accurate in each update but less useful for the online model parameter adaptation to be described later. Our goal, in part, was to find the best batch size through the numerical and experimental exploration in Sec. 5 and Sec. 6.

Two metrics are used to evaluate the model errors in our analysis. The first is the difference between the E-M identified Jacobian, G_{EM} , and the true Jacobian including optical aberrations and influence function biases, G ,

$$\text{Jacobian Error} = \|G_{EM} - G\|_2^2 = \|\Delta G_{EM}\|_2^2, \quad (43)$$

which can be interpreted as the worst case contrast error due to the Jacobian errors with a unit DM command vector. The second metric assumes we are blind to the true Jacobian matrix (which is true in the experiment); we thus reserve part of the data as a validation set. Theoretically, the difference between two neighboring observations with the same probing commands is a function of only the DM commands,

$$\Delta z_k = z_k - z_{k-1} = 4(Gu^p)^T(x_k - x_{k-1}) = 4(Gu^p)^TGu_k, \quad (44)$$

so we can define a validation error of the identified Jacobian matrix, via

$$\begin{aligned} \text{Validation Error} &= \sum_{k=1}^{N_v} \|\Delta z_k - 4(G_{EM}u^p)^T G_{EM}u_k\|_2^2 \\ &= \sum_{k=1}^{N_v} 4\|u^{pT}(G^T G - G_{EM}^T G_{EM})u_k\|_2^2, \end{aligned} \quad (45)$$

where N_v is the number of data steps in the validation set. By definition, the Jacobian error is $\Delta G_{EM} = G_{EM} - G$, so the validation error can be rewritten as,

$$\begin{aligned} \text{Validation Error} &= \sum_{k=1}^{N_v} 4\|u^{pT}(2G^T \Delta G_{EM} + \Delta G_{EM}^T \Delta G_{EM})u_k\|_2^2 \\ &\approx \sum_{k=1}^{N_v} 8\|u^{pT}G^T \Delta G_{EM}u_k\|_2^2, \end{aligned} \quad (46)$$

which is almost proportional to the Jacobian error defined in Eq. 43.

Figure 3 shows the change in the Jacobian errors and the validation errors with respect to the number of data points in the training set. We save the last 500 steps of data for validation, so at most 3500 data points are used as the training set for system identification. As shown in the figure, the validation error curves resemble the Jacobian error curves, validating the utility of this metric for the experiments described in the next section. The identification accuracy primarily depends on the number of data points used for training, no matter whether we use the analytical method or the stochastic gradient ascent algorithm. The stochastic descent algorithm works with a wide range of batch sizes all with similar validation errors, though too small a batch size underperforms compared with others. The analytical method does not work with fewer than 1500 data points

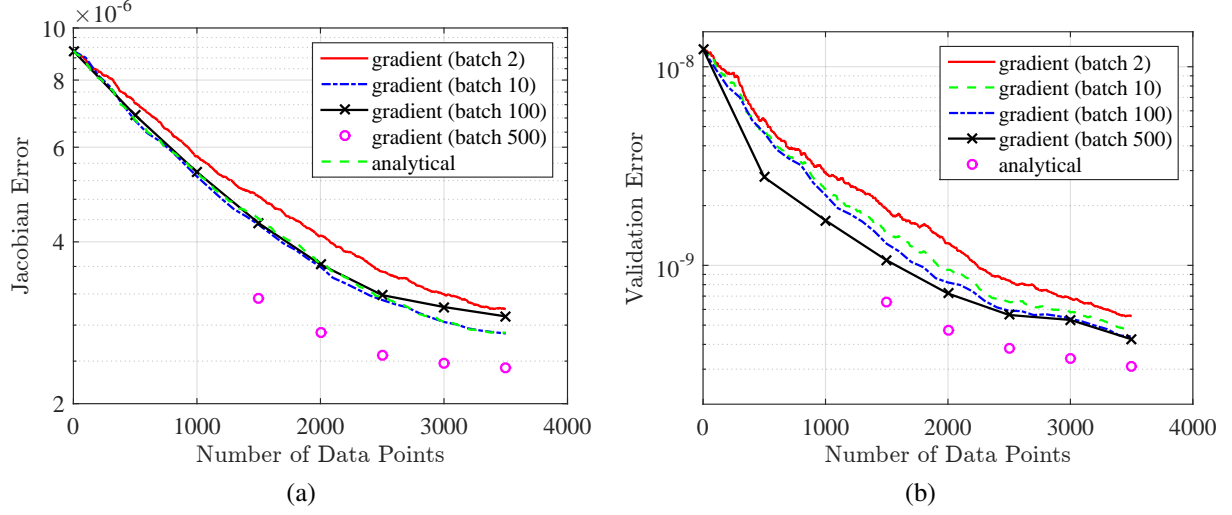


Fig 3 (a) Jacobian errors and (b) validation errors from a simulation over the number of data points in the training set. Different methods, including analytical solutions and stochastic gradient ascent solutions with the batch sizes of 2, 10, 100, and 500 data points are compared using the simulated training data.

because of the ill-posed matrix inversion in Eq. 39 (a). However, it outperforms the gradient ascent once given enough data.

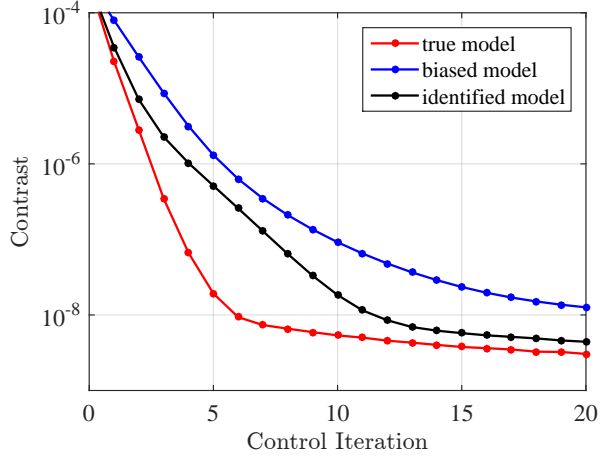


Fig 4 Contrast curves of simulated wavefront correction in HCIL. Biased physics model, true model and identified model using analytical method (3500 data points) are tested respectively.

Figure 4 shows the simulated wavefront correction using the original biased physics model, the true model and the best identified model (analytical solution using 3500 data points). EFC and batch process estimation with two pairs of probing commands are used in this simulation. As can be seen, the identified model beats the biased physics model in both the wavefront control speed and the final contrast. The contrast gap between the true model and the biased model is significantly reduced after the E-M system identification. Since the properties of the wavefront correction always reflect the accuracy of a model, in the following experimental studies, we also use the wavefront correction as a metric to evaluate the models from different amount of data and methods.

6 System identification using the E-M algorithm with experimental data

With the E-M algorithm and the evaluation metrics verified in simulation, we then applied the system identification algorithm on the HCIL testbed experiment. The same sampling policy was used: we ran the wavefront correction to reach a relatively high contrast (settling at around 3×10^{-6}), applied 4000 random DM commands (between -0.6 and 0.6 volts) and collected the resulting difference images, saving the last 500 steps as the validation set. Again, two pairs of DM probes were used for observation at each step. We also compared wavefront control trials using the original physics-based model with the E-M identified models.

6.1 Identification results and wavefront corrections

Figure 5 shows the validation errors for the different cases (analytical solution and gradient ascent with different batch sizes) plotted against the number of data points using the experimental data. The validation error curves decrease with the same trends as in Fig. 3 (b), showing that the E-M algorithm also successfully detects and corrects the Jacobian errors in the experiment.

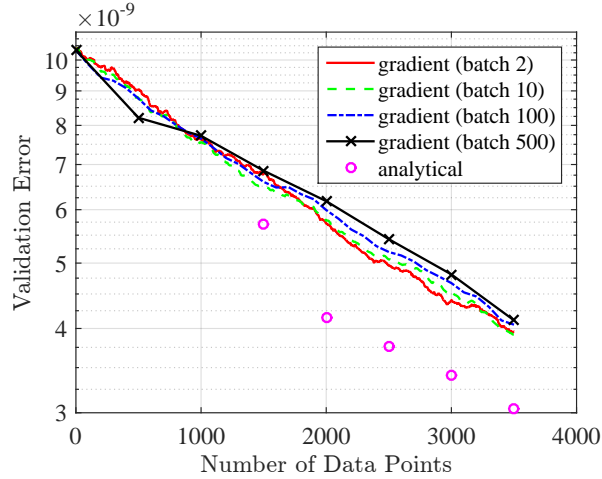


Fig 5 Validation errors in the experiment over the number of data steps in the training set. Different methods, including analytical solutions and stochastic gradient ascent solutions with the batch sizes of 2, 10, 100, 500, are compared using the experimental data.

To further confirm the identified Jacobian accuracy, we compared the wavefront control results using the identified models with the result using the physics model. Although the stochastic optimal control approach described in Section 3 suggest a better approach to incorporating the noises and the Tikhonov regularization, we here used the batch process estimation and EFC with a fixed regularization in all the control experiments so that the control results only depend on the accuracy of the Jacobian matrices. Figure 6 (a) and (b), respectively, show the wavefront control curves (contrast vs. control iteration) using the analytical Jacobian solutions and the gradient ascent Jacobian solutions. In both cases, the wavefront corrections with the identified models are much faster than the physics model in the early stage; they all reached a contrast better than 3×10^{-7} within only four to five control iterations. However, the analytical Jacobians did not perform better than the gradient ascent solutions as expected. After reaching a high contrast, the analytical Jacobians experienced some difficulties in correcting the small residual aberrations, resulting in a final contrast slightly worse than the physics model. We speculate that the analytical E-M solutions

are overfitted to the data noise. In contrast, the gradient ascent solutions reached the same ultimate contrast as the physics model. This is mainly because the achievable final contrast in the lab is currently limited by the scattered, incoherent light. On conclusion from these results is that the gradient method is better for experimental applications. In addition, the wavefront correction did not improve much as the number of data points increased. As analyzed in the following section, this may be because the large model errors, such as the influence function biases, were detected and corrected with only tens of data points. Although more data are beneficial for correcting fine aberrations and avoiding overfitting, their marginal utilities are decreasing.

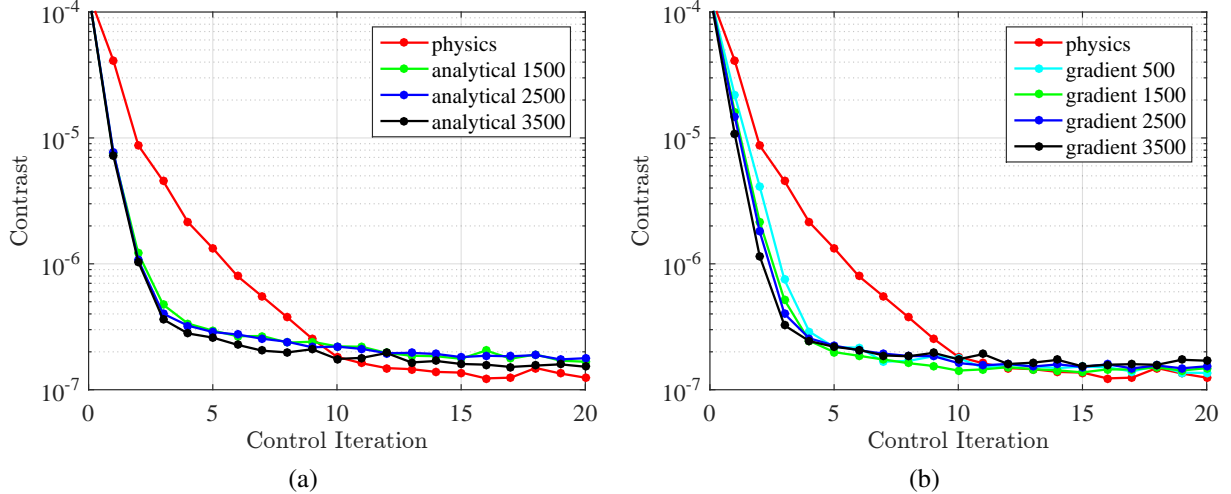


Fig 6 Measured contrast in the HCIL over the control iterations. (a) wavefront corrections using physics model and analytical identified Jacobians with 1500, 2500 and 3500 data points. (b) wavefront corrections using physics model and gradient ascent identified Jacobians (batch size of 500) with 500, 1500, 2500 and 3500 data points.

6.2 Analysis of the sources of Jacobian Errors

In this section we scrutinize the identified Jacobian matrices to explain some of the sources of the Jacobian errors in the HCIL.

The Fourier optics analysis in Eq. 5 shows that the Jacobian errors primarily come from errors in the incident field, \tilde{E}_0 , and the influence functions, $f_{1:N_{act}}$. Thus, in order to diagnose the sources of the Jacobian errors, we can fit our identified Jacobian matrix, G_{EM} , to \tilde{E}_0 and $f_{1:N_{act}}$ in this physics model. After rearranging the real-valued Jacobian matrix, G_{EM} , back into the complex form, F_{EM} , based on Eq. 10, the fitting problem can be formulated as,

$$\min \quad \|F(\tilde{E}_0, f_{1:N_{act}}) - F_{EM}\|_F^2. \quad (47)$$

The incident electric field and influence functions are respectively parameterized as,

$$\begin{aligned} \tilde{E}_0 &= e^{i \sum \beta_m Z_m} \approx 1 + i \sum \beta_m Z_m, \\ f_q &= \rho_q f, \quad \forall q = 1, \dots, N_{act}, \end{aligned} \quad (48)$$

where Z_m and β_m are the Zernike polynomials and their coefficients, f is the shape of the influence function, and ρ_q are the actuator gains. For simplicity, this parameterization neglects amplitude

wavefront aberrations and the difference of influence function shapes among actuators. With this parameterization and expansion in Eq. 48, the fitting problem in Eq.47 becomes a simple linear, least-square regression in the parameters β_m and p_q . To diagnose the quality of the identification, we used the fitted parameters from the identified Jacobian to generate a corresponding fitted Jacobian matrix which only includes the low-order phase aberrations and actuator gain errors.

In Fig. 7, we compare the validation errors of the E-M identified Jacobian matrices and the fitted Jacobian matrices. As shown in Fig. 7 (a), with 3500 data points, the fitted model explains roughly 40 percent of the validation errors whereas the E-M identified model explains roughly 70 percent; our parametrization explain more than half of the gap between the original physics model and our E-M identification results. In particular, the curves from the E-M identified models and the fitted models are close at when the number of data points used is small but gradually diverge, which implies that the low-order wavefront aberrations and DM gain errors are quickly corrected with only a small amount of data.

We further try linear fits on only the Zernike phase polynomials or on the DM gains alone, respectively. As shown in Fig. 7 (b), the DM gains are accurately characterized with only the first 500 data points; the corresponding validation error curves (red) decrease rapidly at the beginning, but change little as the amount of data increases. In contrast, the validation errors from phase aberrations (blue) keep decreasing as the amount of data increases. This indicates that the phase aberrations may be slowly changing over time, so the identification algorithm keeps adjusting the Zernike coefficients as the amount of data increases.

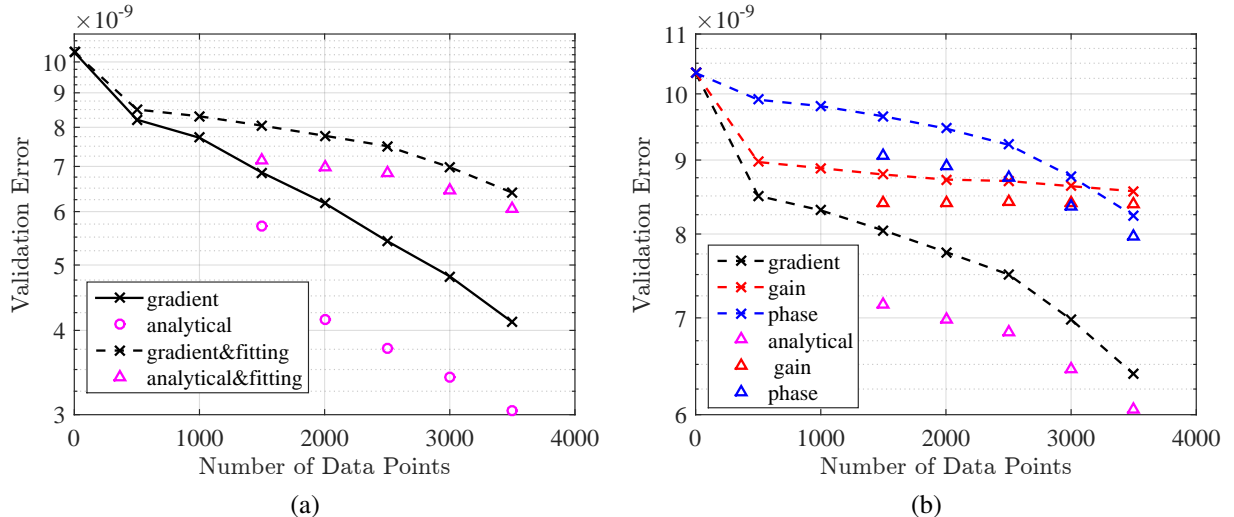


Fig 7 (a) Validation errors of the E-M identified models and the corresponding fitted models. Purple markers and black lines respectively represent the results from the analytical solutions and gradient ascent solutions with batch size of 500. (b) Validation errors of the fitted models that correct only DM gain errors (red), only phase aberrations (blue), and both of them (black). Triangle markers represent the results from the analytical solutions and dashed lines represent the results from the gradient ascent solutions.

The original physics model assumes the same gains for all of the actuators, 5 nm per volt. Figure 8 (a) plots the ratio of the fitted and the original gains given by the gradient ascent identified model using 3500 data points. As can be seen, gains of the actuators in the center change more than the marginal areas. These central actuators (colored yellow) have a profile similar to the ripple

shaped pupil mask, which validates our guess that the unblocked actuators are better characterized by the system identification algorithm. The surrounding actuators are not well characterized (either too large or too small); since they have little influence on the focal plane electric field, their errors do not influence the wavefront correction results. Figure 8 (b) reports the first five fitted Zernike coefficients with respect to the number of data points. The defocus and vertical astigmatism do not change much, while the tip, tilt and oblique astigmatism vary over time, which satisfies our observation that the center of the PSF shifted for one pixel horizontally and vertically respectively in our experiment after collecting 4000 data points. Our E-M identification algorithm successfully tracks these changes in the experiment.

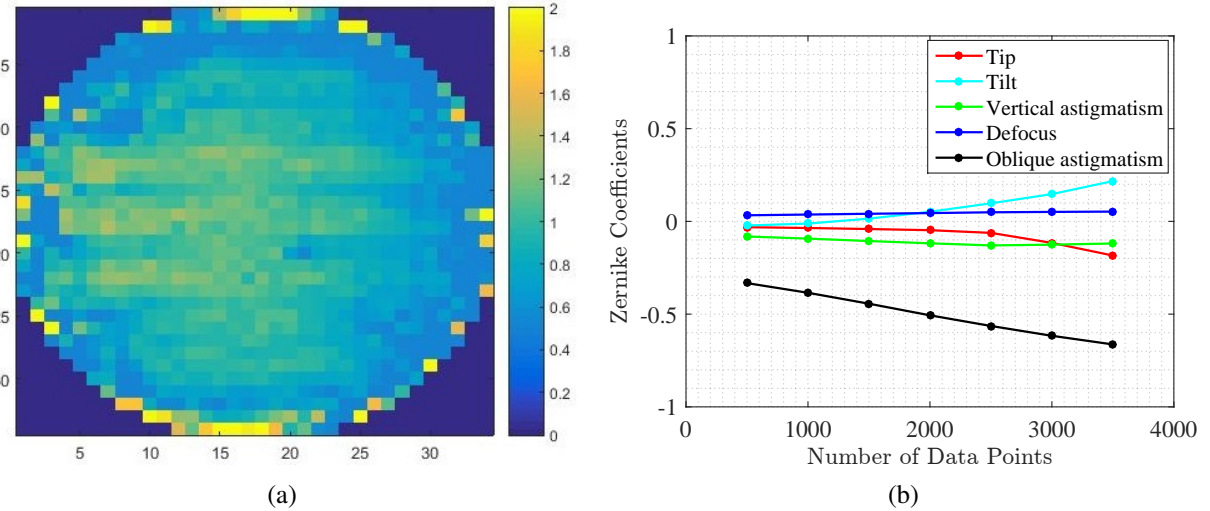


Fig 8 (a) Ratio of the fitted and the original DM gains. (b) First five fitted Zernike coefficients from the identified model using gradient ascent.

We also apply these fitted models to the wavefront corrections. Fig. 9 shows that with only the fitted Jacobian the control is slightly slower to converge than the results in Fig. 6, but the final contrasts remain at the same level as the physics model. Our fitting model sacrifices the ability to diagnose subtle model errors but removes the overfitting noise. As for the case in Fig. 6, more data do not give better results. Based on our analysis above, the reason is likely that the DM gain errors influence the wavefront correction speed but are quickly fixed with only a small amount of data. In addition, the time-varying phase aberrations also preclude the offline identification from improving the wavefront control performance with more data, unless we update the model with small batch size during the wavefront correction. That is explored in the next section.

7 E-M algorithm based adaptive control

The experimental results in Sec. 6 demonstrated the ability of the E-M algorithm to identify the Jacobian errors. However, as also shown there, because of the large data set needed, the E-M identification workflow (data collection - identification - wavefront correction) cannot keep up with some of the most important time-varying errors, such as thermally induced phase aberrations. As a result, a limit is placed on the achievable dark hole generated by the wavefront correction; additional data does not help. In this section, we present a real-time adaptive control framework, or more specifically a reinforcement learning control framework, to solve this problem.

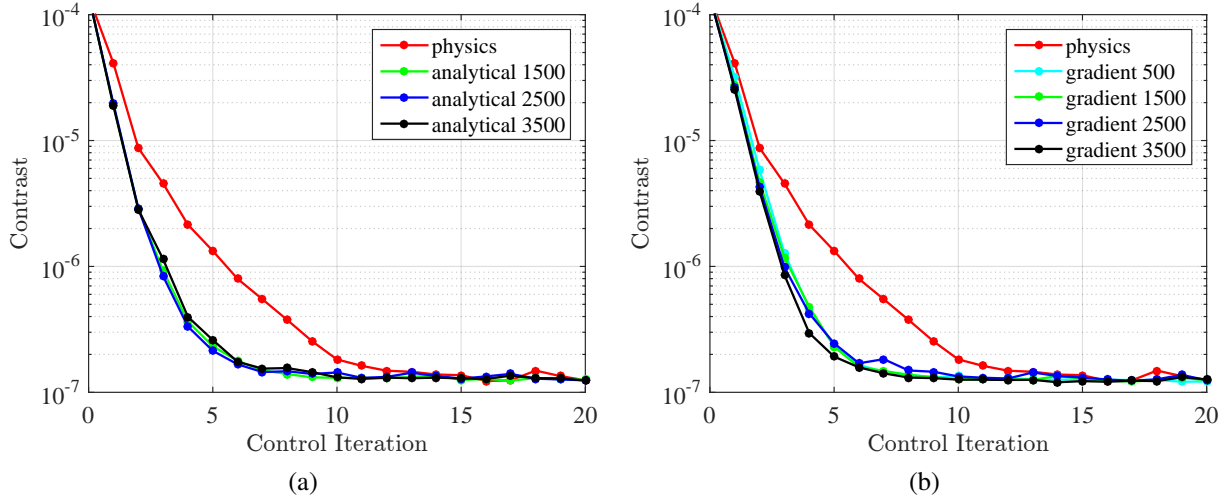


Fig 9 Measured contrast in the HCIL over the control iterations. (a) wavefront corrections using the physics model and the fitted models (DM gains and Zernike phase aberrations) from analytical identified Jacobians. (b) using the physics model and the fitted models (DM gains and Zernike phase aberrations) from gradient ascent identified Jacobians.

7.1 Reinforcement learning for FPWC

Reinforcement learning control has attracted much attention recently as an important branch of machine learning. In reinforcement learning, the system, or agent, alternately runs a control policy to explore the environment and an adaptation step that varies the policy based on the information from the control step. Since the agents directly learn from the control attempts, it is more efficient for them to find the best control policies and track the model variations. This technique has been widely applied to training complex control systems, such as those playing the game of Go²⁷ or video games,²⁸ robot manipulation, motion planning, and locomotion.²⁹

Figure 10 shows the block diagram of an adaptive FPWC system. It combines the wavefront estimation and control with the E-M system identification presented in Sec. 4. In this scheme, we no longer use random DM commands for identification. Instead, the DM commands and resulting images from the control loops are used as the training data for the E-M model identification. The new adaptive FPWC system now loops between running steps of wavefront estimation and control and updating the model parameters (which also means updating the control and estimation policy) using the EM algorithm.

In addition, not only is the Jacobian matrix, G , identified in the adaptive/reinforcement learning control step, so too are the process noise, σ^2 , and observation noise, ν^2 as demonstrated in Eq. 40 and Eq. 41. These are then used to tune the wavefront estimator (the covariance matrices of process noises and observation noises in Kalman filter) and controller (Tikhonov regularization matrix in EFC) based on Eq. 31, Eq. 32 and Eq. 27.³ As a result, the Kalman filter estimator better balances the weights of the model predictions and observations, and the controller better chooses the damping parameter in the wavefront correction.

³In our software implementation, we introduce a hyperparameter, γ , to Eq. 27, which defines a modified regularization matrix, $W' = \gamma W = 2\gamma N_{pix} \sigma^2 \mathbb{I}$, because we found the controller is usually able to be more aggressive than the theoretical suggestion.

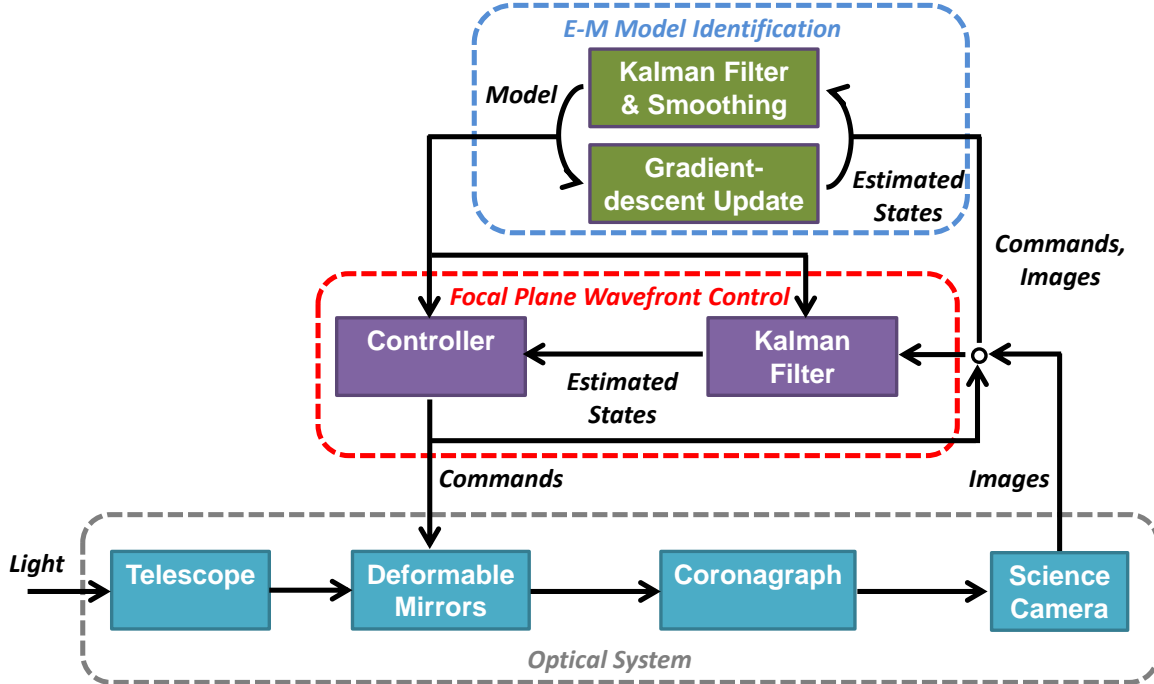


Fig 10 Block diagram of the E-M algorithm based adaptive focal plane wavefront correction (FPWC) system.

7.2 Reinforcement learning simulation

Again using the imperfect lab conditions that result in phase aberrations and influence function biases as stated in Sec. 5.1, we simulated the reinforcement learning control for 50 control iterations. Two pairs of probing images were collected at each iteration for wavefront estimation. In Sec. 5 and Sec. 6, we use same pair-wise probes for the convenience of validation error calculation, however, we allow the DM probes to vary among different control iterations in the reinforcement learning control simulation. After every 10 control iterations, we supply the 10 control commands, the pair-wise probes (2 pairs/step \times 10 steps) and the camera images (2 images/pair \times 2 pairs/step \times 10 steps) to the E-M algorithm to update the Jacobian matrix and the tuning parameters in the estimator and controller. For comparison, the wavefront control with the true Jacobian model and the fixed biased Jacobian model were also simulated. In both of these benchmark cases, the Kalman filter and the EFC controller were tuned manually. Figure 11 shows the results of the three simulations. As can be seen, the reinforcement learning control gradually closed the contrast gap between the biased model and the true model. The E-M adaptation at every ten iterations can be clearly seen on the correction curves.

7.3 Reinforcement learning experiment in HCIL

In this section we present the results of using the reinforcement learning adaptive control approach in the HCIL. Unfortunately, because the ultimate contrast achievable in the HCIL is limited to roughly 1.5×10^{-7} due to incoherent background light (as seen in Figs. 6 and 9), it is not possible to reproduce the simulation results from the previous section. There, the adaptation step was run after each 10 iterations of the control. But as can be seen in Fig. 11, the modeled system reaches a contrast better than the lab limit of 10^{-7} in fewer than 10 steps, before the first reinforcement learning step. Through trial and error it was found that the E-M algorithm cannot robustly identify

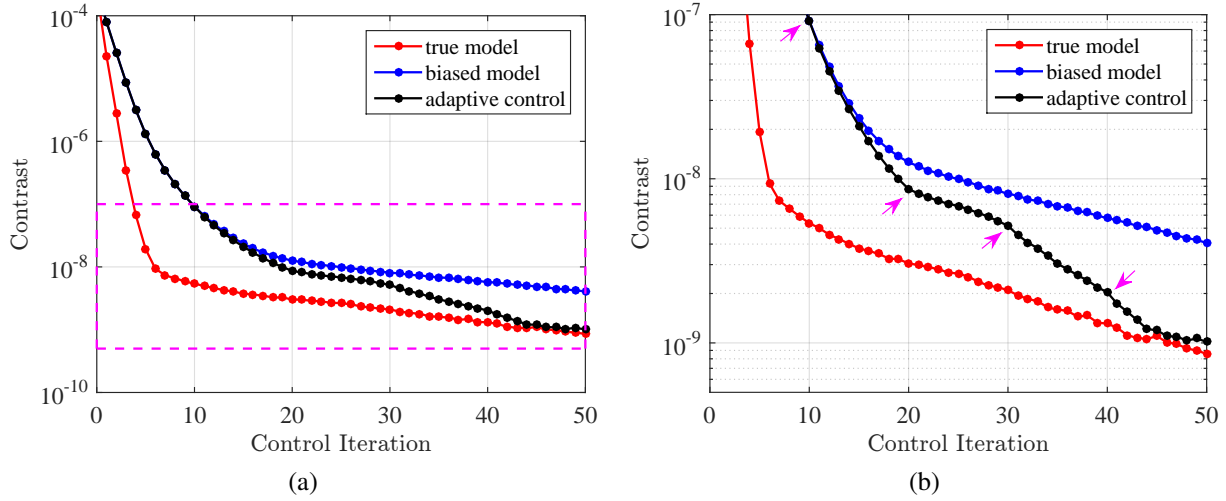


Fig 11 (a) Simulated FPWC reinforcement learning control and the benchmark wavefront control with the true Jacobian matrix and the fixed biased Jacobian matrix. The model parameters are updated using the E-M algorithm every ten iterations. (b) Zoomed-in figure of the box region in (a). The E-M identifications occurred at the iterations marked by pointed arrows.

the system with fewer than 10 learning steps. Therefore, to experimentally verify the algorithm, we limited each FPWC run to 10 control iterations and updated the model parameters using the E-M algorithm after each trial. The Jacobian and tuning parameters were then used for the next trial of wavefront correction.

As shown in Fig. 12 (a), the rate of convergence of the wavefront correction became faster after each learning trial. Note that we ran the E-M identification after every learning iteration, however, to keep the figure clean, we only report a few of the typical results (wavefront control with the initial biased model and after 1, 5, 10, 15, 19 learning trials). After only 19 learning trials, the FPWC system was able to reach 1×10^{-6} in one control step and below 2×10^{-7} contrast in three control steps, which is faster than the results from the off-line system identification. Figs. 12 (b) (c) (d) show the changes in the estimates of process noise and observation noise covariances and their ratio at each learning trial. As shown in these figures, we underestimated the noise levels at the beginning. The adaptive controller quickly corrected these incorrect assumptions. Then, the adaptive controller gradually corrected the errors in the Jacobian matrix, so that the process and observation noise covariance estimates decreased with additional learning trials. More details about the adaptive control experiment can be seen in the video in Fig. 13.

By using this reinforcement learning approach, much effort is saved, and accuracy gained, by not having to take testbed layout measurements, perform phase retrieval and surface characterization, or having to manually tune the controller and estimator parameters. The reinforcement learning adaptive control results also shows promise for enabling self-maintenance of the FPWC during the mission.

8 Conclusion and future work

Efficient and successful focal plane wavefront control and estimation in coronagraph instruments requires accurate modeling of the optical system. In this work, we proposed an expectation-maximization (E-M) algorithm to identify the optical system as a linear state-space model. Accord-

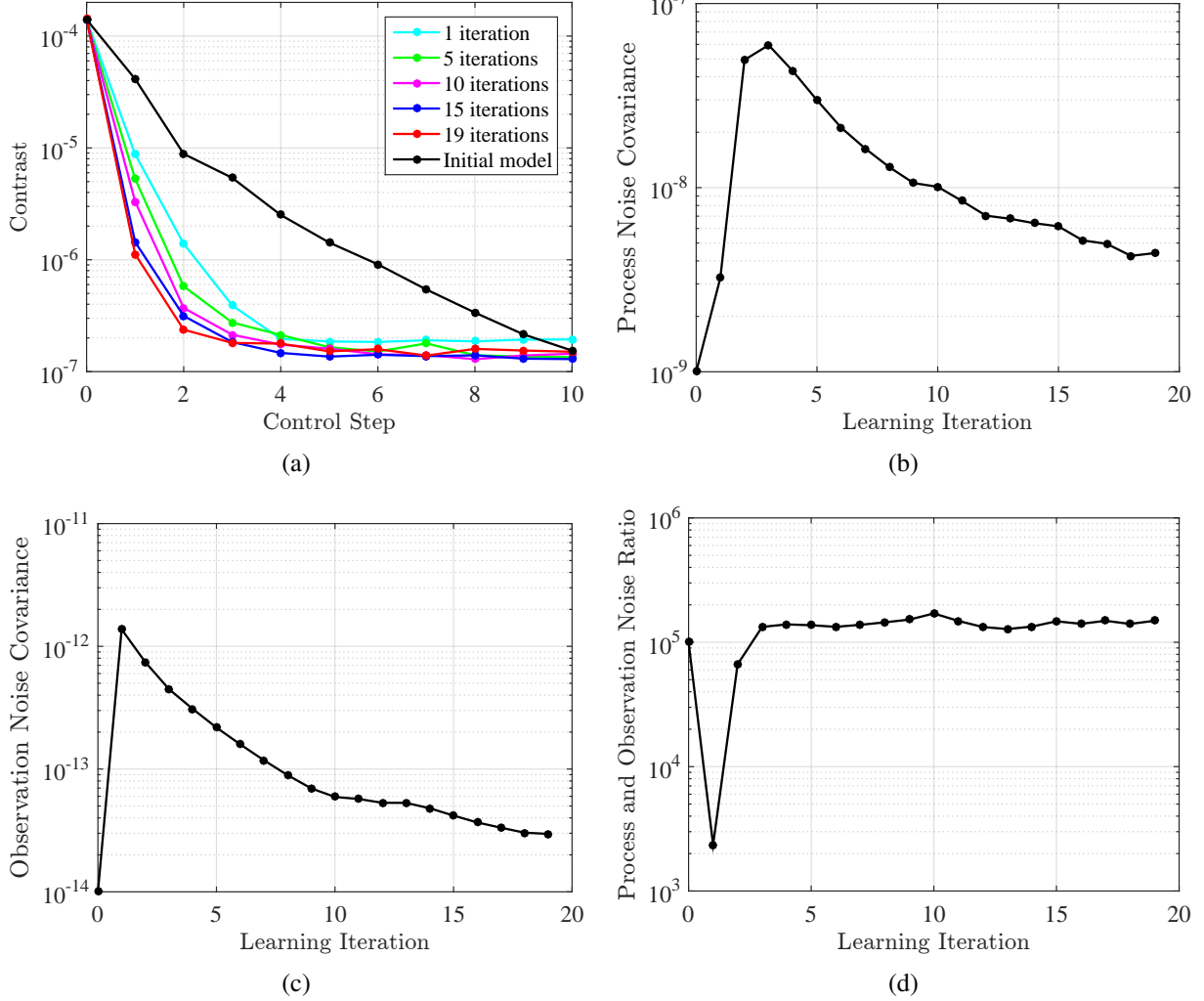


Fig 12 Change of (a) the wavefront correction speed, (b) the process noise, (c) the observation noise and (d) the process and observation noise ratio with respect to the learning iterations. To compare the wavefront correction speed, we present the measured contrast over 10 control iterations for the initial model and identified model after 1, 5, 10, 15, 19 learning iterations.

ing to the simulation and experimental results in the Princeton HCIL, the algorithm successfully corrects model errors such as those produced from errors in the DM gains and initial phase aberrations. Use of the identified models significantly increases the rate at which the wavefront correction converges. We further developed a model based adaptive/reinforcement learning control scheme based on this E-M algorithm. The adaptive controller alternates between the wavefront correction and the controller and estimator self-tuning, which significantly improves the performance of both the estimator and controller and requires only tens of learning iterations. This approach is very promising for the automatic maintenance of the FPWC system in future space missions.

Future work will focus on generalizing this frame work with more realistic assumptions. First, we plan to identify the full matrix regularization suggested in Sec. 3 instead of the scalar regularization. This will help us understand the inter-actuator couplings that are neglected by electric field conjugation and stroke minimization, as well as improve the performance of the wavefront

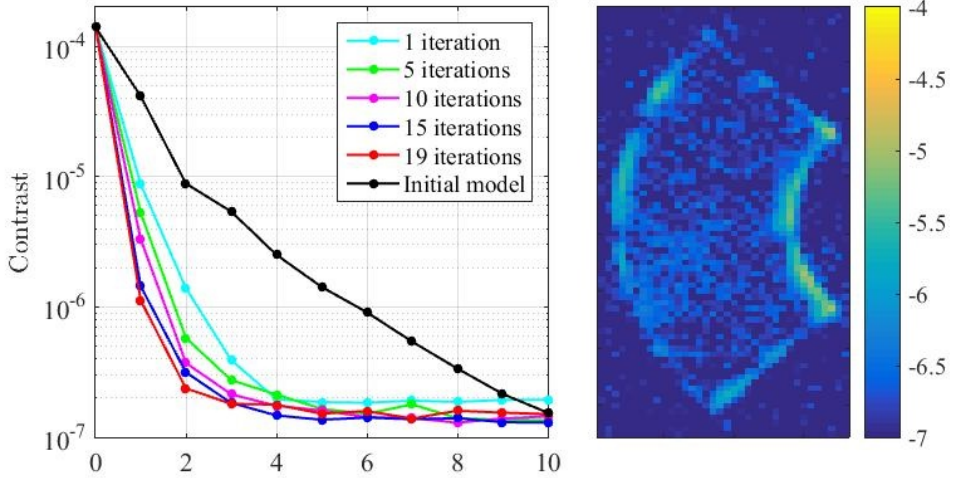


Fig 13 A still image from the video about the adaptive wavefront correction in HCIL. (MP4, 3.34 MB)

correction. Second, we also plan to drop the linearity assumption and approximate the optical system and the wavefront controller and estimator using neural networks. By introducing system nonlinearities back into the model, we should be able to further increase the speed and efficiency of the wavefront corrections, gain a deeper contrast, and better extract the exoplanet signal.

Acknowledgments

This work was performed under contract to the Jet Propulsion Laboratory of the California Institute of Technology, award number AWD1004079, and under contract to NASA Goddard Space Flight Center, award number AWD1004730.

References

- 1 N. J. Kasdin, R. J. Vanderbei, D. N. Spergel, *et al.*, “Extrasolar planet finding via optimal apodized-pupil and shaped-pupil coronagraphs,” *The Astrophysical Journal* **582**(2), 1147 (2003).
- 2 J. Trauger, D. Moody, B. Gordon, *et al.*, “A hybrid lyot coronagraph for the direct imaging and spectroscopy of exoplanet systems: recent results and prospects,” Society of Photo-Optical Instrumentation Engineers (SPIE) (2011).
- 3 O. Guyon, “Phase-induced amplitude apodization of telescope pupils for extrasolar terrestrial planet imaging,” *Astronomy & Astrophysics* **404**(1), 379–387 (2003).
- 4 N. T. Zimmerman, A. E. Riggs, N. J. Kasdin, *et al.*, “Shaped pupil lyot coronagraphs: high-contrast solutions for restricted focal planes,” *Journal of Astronomical Telescopes, Instruments, and Systems* **2**(1), 011012–011012 (2016).
- 5 C. Vérinaud, M. Le Louarn, V. Korkiakoski, *et al.*, “Adaptive optics for high-contrast imaging: pyramid sensor versus spatially filtered shackhartmann sensor,” *Monthly Notices of the Royal Astronomical Society: Letters* **357**(1), L26–L30 (2005).
- 6 R. Frazin, “Fast, nonlinear phase estimation with the non-modulated pyramid wavefront sensor at low strehl ratio,” *arXiv preprint arXiv:1708.09044* (2017).
- 7 B. Macintosh, J. R. Graham, P. Ingraham, *et al.*, “First light of the gemini planet imager,” *Proceedings of the National Academy of Sciences* **111**(35), 12661–12666 (2014).

- 8 D. Spergel, N. Gehrels, C. Baltay, *et al.*, “Wide-field infrared survey telescope-astrophysics focused telescope assets wfirst-afta 2015 report,” *arXiv preprint arXiv:1503.03757* (2015).
- 9 M. C. Noecker, F. Zhao, R. Demers, *et al.*, “Coronagraph instrument for wfirst-afta,” *Journal of Astronomical Telescopes, Instruments, and Systems* **2**(1), 011001–011001 (2016).
- 10 J. R. Fienup, “Phase retrieval algorithms: a comparison,” *Applied optics* **21**(15), 2758–2769 (1982).
- 11 Y. Shechtman, Y. C. Eldar, O. Cohen, *et al.*, “Phase retrieval with application to optical imaging: a contemporary overview,” *IEEE signal processing magazine* **32**(3), 87–109 (2015).
- 12 C. M. Prada, L. Yao, Y. Wu, *et al.*, “Characterization of low-mass deformable mirrors and asic drivers for high-contrast imaging,” in *Techniques and Instrumentation for Detection of Exoplanets VIII*, **10400**, 1040011, International Society for Optics and Photonics (2017).
- 13 P. J. Bordé and W. A. Traub, “High-contrast imaging from space: speckle nulling in a low-aberration regime,” *The Astrophysical Journal* **638**(1), 488 (2006).
- 14 A. Giveon, B. Kern, and S. Shaklan, “Pair-wise, deformable mirror, image plane-based diversity electric field estimation for high contrast coronagraphy,” in *Proc. SPIE*, **8151**, 815110 (2011).
- 15 T. D. Groff and N. J. Kasdin, “Kalman filtering techniques for focal plane electric field estimation,” *JOSA A* **30**(1), 128–139 (2013).
- 16 A. E. Riggs, N. J. Kasdin, and T. D. Groff, “Recursive starlight and bias estimation for high-contrast imaging with an extended kalman filter,” *Journal of Astronomical Telescopes, Instruments, and Systems* **2**(1), 011017–011017 (2016).
- 17 A. Give’on, B. Kern, S. Shaklan, *et al.*, “Broadband wavefront correction algorithm for high-contrast imaging systems,” in *Astronomical Adaptive Optics Systems and Applications III*, **6691**, 66910A, International Society for Optics and Photonics (2007).
- 18 L. Pueyo, J. Kay, N. J. Kasdin, *et al.*, “Optimal dark hole generation via two deformable mirrors with stroke minimization,” *Applied optics* **48**(32), 6296–6312 (2009).
- 19 T. D. Groff, A. E. Riggs, B. Kern, *et al.*, “Methods and limitations of focal plane sensing, estimation, and control in high-contrast imaging,” *Journal of Astronomical Telescopes, Instruments, and Systems* **2**(1), 011009–011009 (2016).
- 20 D. Marx, B.-J. Seo, B. Kern, *et al.*, “Electric field conjugation in the presence of model uncertainty,” in *Techniques and Instrumentation for Detection of Exoplanets VIII*, **10400**, 104000P, International Society for Optics and Photonics (2017).
- 21 D. Marx and B. Kern, “Phase retrieval implementation for the wfirst coronagraph development testbed,” in *Computational Optical Sensing and Imaging*, CT4C-4, Optical Society of America (2016).
- 22 H. Zhou, B. Nemati, J. Krist, *et al.*, “Closing the contrast gap between testbed and model prediction with wfirst-cgi shaped pupil coronagraph,” in *Space Telescopes and Instrumentation 2016: Optical, Infrared, and Millimeter Wave*, **9904**, 990419, International Society for Optics and Photonics (2016).
- 23 H. Sun, N. J. Kasdin, R. Vanderbei, *et al.*, “Improved high-contrast wavefront controllers for exoplanet coronagraphic imaging systems,” in *Techniques and Instrumentation for Detection of Exoplanets VIII*, **10400**, 104000R, International Society for Optics and Photonics (2017).

- 24 H. Sun, N. J. Kasdin, and R. Vanderbei, “Identification of the focal plane wavefront control system using em algorithm,” in *Techniques and Instrumentation for Detection of Exoplanets VIII*, **10400**, 1040028, International Society for Optics and Photonics (2017).
- 25 A. P. Dempster, N. M. Laird, and D. B. Rubin, “Maximum likelihood from incomplete data via the em algorithm,” *Journal of the royal statistical society. Series B (methodological)* , 1–38 (1977).
- 26 Z. Ghahramani and G. E. Hinton, “Parameter estimation for linear dynamical systems,” tech. rep., Technical Report CRG-TR-96-2, University of Totronto, Dept. of Computer Science (1996).
- 27 D. Silver, A. Huang, C. J. Maddison, *et al.*, “Mastering the game of go with deep neural networks and tree search,” *Nature* **529**(7587), 484–489 (2016).
- 28 V. Mnih, K. Kavukcuoglu, D. Silver, *et al.*, “Playing atari with deep reinforcement learning,” *arXiv preprint arXiv:1312.5602* (2013).
- 29 J. Kober, J. A. Bagnell, and J. Peters, “Reinforcement learning in robotics: A survey,” *The International Journal of Robotics Research* **32**(11), 1238–1274 (2013).

He Sun is a PhD candidate of Mechanical and Aerospace Engineering at Princeton University. He received his B.S. degree in Engineering Mechanics and Economics from Peking University in 2014. His research interests include coronagraph design and adaptive optics for exoplanet imaging, optimal control and estimation, statistical learning, and robotics. He is a member of the American Astronomical Society and the SPIE.

N. Jeremy Kasdin is a Professor of Mechanical and Aerospace Engineering at Princeton University. He is the Principal Investigator of Princeton’s High Contrast Imaging Laboratory and Coronagraph Adjutant Scientist for WFIRST, the Wide Field InfraRed Survey Telescope. He received his Ph.D. from Stanford University in 1991. Professor Kasdin’s research interests include space systems design, space optics and exoplanet imaging, orbital mechanics, guidance and control of space vehicles, optimal estimation, and stochastic process modeling. He is an Associate Fellow of the American Institute of Aeronautics and Astronautics and member of the American Astronomical Society and the SPIE.

Robert Vanderbei is a Professor of Operations Research and Financial Engineering at Princeton University. He also holds courtesy appointments in the Department of Mathematics, Astrophysics, Computer Science, and Mechanical and Aerospace Engineering. He received his Ph.D. from Cornell University in 1981. He is a Fellow of the American Mathematical Society (AMS), the Society for Applied and Industrial Mathematics (SIAM) and the Institute for Operations Research and the Management Sciences (INFORMS).

List of Figures

- 1 Telescope optical system architecture and focal plane wavefront control loop. System variables are also marked on the diagram, where \tilde{E}_0 is the incident pupil plane electric field, $\Delta\phi_m$ is the DM surface phase change at a single step, $\mathcal{C}\{\cdot\}$ represents the light propagation through coronagraph, E_k is the focal plane electric field, I_k represents the camera images, u_k represents the DM commands, and \hat{E}_k/\hat{x}_k are the estimated complex/real-valued states of electric field.
- 2 Layout of the HCIL testbed. Rippled shaped pupil and bowtie shaped focal plane mask are applied to suppress the contrast in the focal plane. Two Boston Micro-Machines MEMS DMs are installed for focal plane wavefront correction.
- 3 (a) Jacobian errors and (b) validation errors from a simulation over the number of data points in the training set. Different methods, including analytical solutions and stochastic gradient ascent solutions with the batch sizes of 2, 10, 100, and 500 data points are compared using the simulated training data.
- 4 Contrast curves of simulated wavefront correction in HCIL. Biased physics model, true model and identified model using analytical method (3500 data points) are tested respectively.
- 5 Validation errors in the experiment over the number of data steps in the training set. Different methods, including analytical solutions and stochastic gradient ascent solutions with the batch sizes of 2, 10, 100, 500, are compared using the experimental data.
- 6 Measured contrast in the HCIL over the control iterations. (a) wavefront corrections using physics model and analytical identified Jacobians with 1500, 2500 and 3500 data points. (b) wavefront corrections using physics model and gradient ascent identified Jacobians (batch size of 500) with 500, 1500, 2500 and 3500 data points.
- 7 (a) Validation errors of the E-M identified models and the corresponding fitted models. Purple markers and black lines respectively represent the results from the analytical solutions and gradient ascent solutions with batch size of 500. (b) Validation errors of the fitted models that correct only DM gain errors (red), only phase aberrations (blue), and both of them (black). Triangle markers represent the results from the analytical solutions and dashed lines represent the results from the gradient ascent solutions.
- 8 (a) Ratio of the fitted and the original DM gains. (b) First five fitted Zernike coefficients from the identified model using gradient ascent.
- 9 Measured contrast in the HCIL over the control iterations. (a) wavefront corrections using the physics model and the fitted models (DM gains and Zernike phase aberrations) from analytical identified Jacobians. (b) using the physics model and the fitted models (DM gains and Zernike phase aberrations) from gradient ascent identified Jacobians.
- 10 Block diagram of the E-M algorithm based adaptive focal plane wavefront correction (FPWC) system.

- 11 (a) Simulated FPWC reinforcement learning control and the benchmark wavefront control with the true Jacobian matrix and the fixed biased Jacobian matrix. The model parameters are updated using the E-M algorithm every ten iterations. (b) Zoomed-in figure of the box region in (a). The E-M identifications occurred at the iterations marked by pointed arrows.
- 12 Change of (a) the wavefront correction speed, (b) the process noise, (c) the observation noise and (d) the process and observation noise ratio with respect to the learning iterations. To compare the wavefront correction speed, we present the measured contrast over 10 control iterations for the initial model and identified model after 1, 5, 10, 15, 19 learning iterations.
- 13 A still image from the video about the adaptive wavefront correction in HCIL. (MP4, 3.34 MB)

List of Tables